scientific reports

Check for updates

OPEN

Vascular insult in neonatal retinal hemorrhage: computational analysis of a fundus-segmented blood vessel network

Matthew R. Lam[1,5], Jose A. Colmenarez[3,5], Pengfei Dong[3], Linxia Gu[3]✉ & Donny W. Suh[2,4]✉

Common hypotheses for the biomechanical cause underlying neonatal retinal hemorrhage include elevated intracranial pressure (ICP) inducing venous outflow obstruction and retinal deformation. A finite element computational model of the eye, optic nerve, and orbit was simulated with particular attention to the retinal vessels to analyze stress and strain on these structures during external head compression associated with normal vaginal delivery. Pressure from maternal contractions displaced the eye backward into the orbit, and the stiff optic nerve sheath provided localized resistance to this posterior displacement at its insertion point, resulting in tensile strain of 2.5% in the peripapillary (central) retina. Correspondingly, retinal vessels experienced tensile stress of up to 2.3 kPa near the optic nerve insertion point and opposing compressive stress of up to 3.2 kPa further away. The optic nerve was longitudinally compressed and experienced a mean radial tensile strain of 2.0%. Overall, forces associated with maternal labor resulted in a pattern of eye deformation that stretched the central retina in this simulation, mirroring the classical posterior localization of neonatal retinal hemorrhage. The optic nerve increased modestly in diameter despite rising ICP, suggesting retinal deformation is a more likely mechanism for retinal hemorrhage than occlusion of the central retinal vein.

Keywords Retinal hemorrhage, Neonate, Normal vaginal delivery, Computer simulation, Finite element

As many as half of all neonates are born with benign, physiological retinal hemorrhage[1]. These hemorrhages are classically characterized as intraretinal (occurring within the layers of the retina as opposed to in front or behind), centrally localized (appearing in the center of the retina at the back, or posterior, of the eye), and self-resolving within weeks with no long-term consequences[2,3]. Despite the innocuous nature of physiologic neonatal retinal hemorrhage, cases must be differentiated from other causes of retinal hemorrhages in neonates, including the medical and legally significant abusive head trauma. Consideration of maternal risk factors of neonatal retinal hemorrhage is important when weighing the likelihood of the underlying causes, especially the mode of delivery. Retinal hemorrhage has been reported in approximately 25–34% of infants born by normal vaginal delivery (NVD), 35–50% of infants when instruments are used to assist delivery, particularly vacuum suction, and 7–10% when Cesarean section is performed[4,5]. These differing rates of incidence led many to hypothesize that the mechanism driving physiologic neonatal retinal hemorrhage is related to changes in intracranial pressure during childbirth.

Current methods of performing fetal analysis during labor in vivo are prohibitively invasive, making testing of any hypothesis challenging. One well-documented alternative is the use of high fidelity computer simulations, such as finite element analysis (FEA), which has been used extensively to study the eye during trauma or other circumstances in which conventional methods would not be feasible[6–9]. In FEA simulations, hundreds of

[1]Creighton University School of Medicine Phoenix Regional Campus, Phoenix, AZ 85012, USA. [2]Gavin Herbert Eye Institute, University of California, Irvine, Irvine, CA 92617, USA. [3]Department of Biomedical Engineering and Science, Florida Institute of Technology, Melbourne, FL 32901, USA. [4]Department of Ophthalmology and Visual Sciences, Irvine School of Medicine, Gavin Herbert Eye Institute, University of California, Irvine, CA 92697, USA. [5]These authors contributed equally: Matthew R. Lam and Jose A. Colmenarez. ✉email: gul@fit.edu; donnys@hs.uci.edu

thousands to millions of modular elements of varying shapes and sizes can be arranged to create high resolution three-dimensional model of a given organ, such as the eye. Then, physiologic material properties of various human tissue can be assigned to each element. The model can finally be exposed to external forces replicating clinical scenarios, during which it visualizes and quantifies biomechanical endpoints like deformation, pressure and stress at each element, ultimately providing a uniquely detailed representation of the simulated event. FEA simulations have become an invaluable tool in evaluating ocular trauma, with models becoming more refined with successive experiments. However, continuously increasing the fidelity of the model also increases computational expenses and time horizon, limiting iterative experimentation.

FEA simulations of the eye have previous been conducted to study neonatal retinal hemorrhage in NVD and made inferences from macroscopic observations, but were unable to directly visualize the vasculature and study their biomechanics and blood flow[6]. The purpose of this investigation is therefore to improve upon prior these FEA experiments with novel implementation of simulation techniques to overcome computational barriers and achieve a more intuitive and visual representation of the retinal vasculature during childbirth. Direct simulation of the retinal vessels will not only bolster understanding of the pathogenesis of neonatal retinal hemorrhage but will also demonstrate methods to increase computational efficiency and their applications in ophthalmic research.

Methods

We developed a series of numerical models to assess the biomechanical response of the retinal vasculature subjected to fetal head compression during NVD. First, we investigated the variations in intraocular pressure (IOP) (pressure within the eye) and intracranial pressure (ICP) (pressure within the skull) by conducting a parametric study on an axisymmetric model of the eye that considered a range of extracranial pressure (ECP) exerted by the uterus and the durations of contractions. Resulting values were then applied to examine the stress on neonatal retinal vessels and their susceptibility to rupture using a full three-dimensional model of the eye and orbit, the bony socket within which the eye and related structures reside. Precise geometric characteristics of the vasculature were acquired by applying image processing techniques to segment and enhance the retinal vessels from a fundus image. Lastly, we investigated the effect of heightened ICP on the optic nerve, the nerve that connects the eye to the brain. A layer of continuous connective tissue envelops both the brain and optic nerve, known as the meninges and optic nerve sheath respectively, with cerebrospinal fluid filling the space between. Therefore, increases in ICP are transmitted to the optic nerve via this communication[10]. The details of these assessments are elaborated upon in the subsequent sections.

Axisymmetric model and parametric study

The implicit FEA solver from ABAQUS/Standard 2023 (Dassault Systemes Simulia Corp., Providence, RI, USA) was used to evaluate the dynamic response of a simulated eye and orbit model. For rapid computation of the NVD simulation, we developed an axisymmetric model of the orbit that takes advantage of the eye's rotational symmetry to focus the analysis in a two-dimensional cross section (Fig. 1C). This substantially reduced the number of elements and therefore demand for computational resources while still maintaining the accuracy of the results. The aqueous humor and vitreous humor within the eye and cerebrospinal fluid within the optic nerve sheath were modeled as hydrostatic fluids, where the pressure gradient in their respective cavities is considered negligible. Further, the hydrostatic elements were only distributed along the boundary of the cavity, eliminating the need for additional elements to fill it entirely. The rest of the eye tissues were modeled as isotropic hyperelastic materials to capture their inherent non-linear stress–strain behavior. Additional viscoelastic properties were incorporated into the orbital adipose (fat) tissue to represent its response to strain-rate dependencies during contraction. Table 1 displays a summary of the involved tissues and their properties. Finally, fixed constraints were applied to the intracanalicular boundary at the back of the model to mimic the stationary position of the orbit within the skull.

During simulation of NVD, a uniform force derived from physiologic ECP was exerted over the anterior (front) pole of the model to represent the pressure load transmitted by the birth canal. To replicate the gradual onset and offset of uterine contractions, the ECP underwent a linear increase for the first half of the contraction duration, followed by a smooth transition towards a linear release during the second half.

This axisymmetric model was used to perform a parametric study examining the effects of varying pressures and contraction durations. The involved parameters, IOP, ICP, ECP, and contraction time, were sampled using a Latin hypercube sampling (LHS) scheme to ensure an even sparseness of data points within a normally distributed range of study. In contrast to alternative quasi-random sampling techniques, LHS allows for a more efficient exploration of the parameters and their interactions, thereby decreasing the requisite number of simulations. Table 2 displays the means and standard deviations used for sampling the parameters as reported in the literature.

A total of 100 NVD scenarios were sampled for simulation to guarantee an optimal representation of the parameter space. The changes in both IOP and ICP, as well as the stresses on the optic nerve, were recorded for each simulation run. The parametric sampling, FE model creation, and result acquisition were automatically executed by Python code integrated with the scripting interface in ABAQUS[11–22].

Retinal vessel segmentation

To investigate blood vessel wall behavior, we performed vessel segmentation, i.e., extraction of precise vessel geometry from an image for implementation into the FE model, on a fundus photo featuring moderate intraretinal hemorrhage in a vaginally delivered neonate (Fig. 2A). Vessels with a minimum length of 15 pixels were automatically segmented following the filtering method proposed by Soares et al. via MATLAB[23]. First, we preprocessed the colored image by extracting the green channel from its RGB components to maximize vessel contrast against the background of retinal tissue. Then, we progressively expanded the boundaries of the

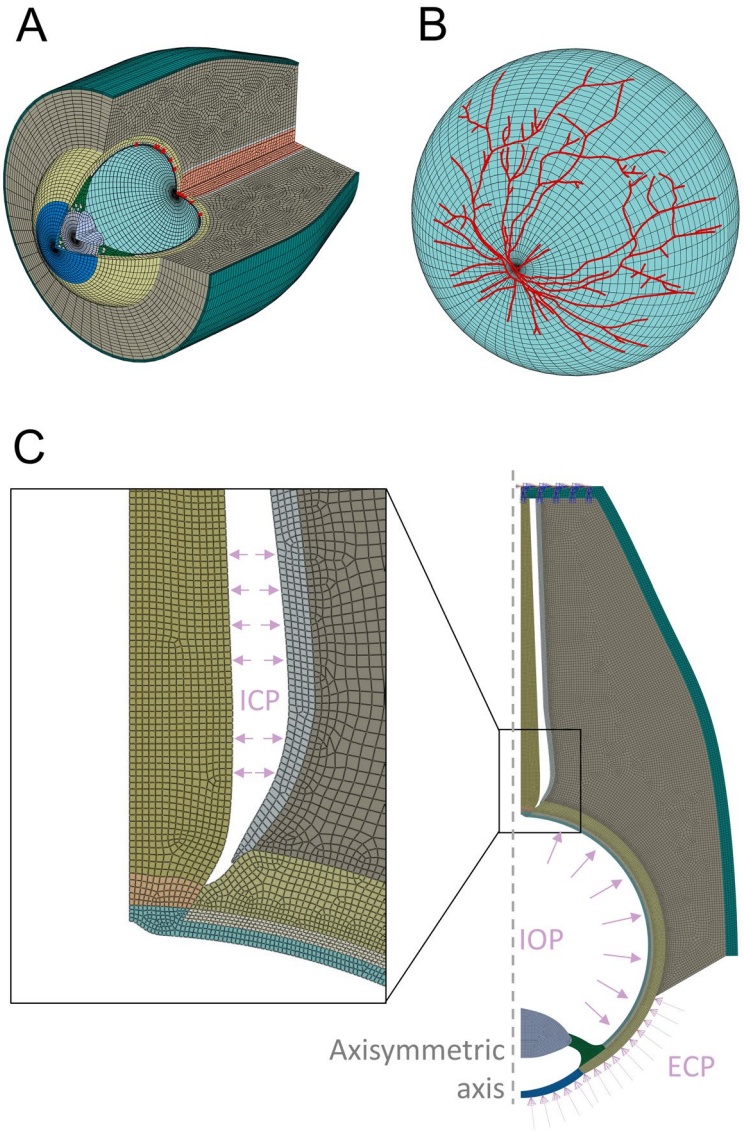

Fig. 1. Three-dimensional FEA model of the eye and orbit with embedded retinal vessels (**A**) Isometric anterolateral (from the front and side) view of the model with cross section. (**B**) Anterolateral cross section of the posterior (at the back of the eye) retina (blue) with embedded vessel elements (red). (**C**) Two-dimensional axisymmetric model derived from the full-scale three-dimensional model. Insert highlights the optic nerve sheath and its contents.

aperture to mitigate the pronounced contrast stemming from the external black regions. This involved iteratively replacing each pixel along the border with the average pixel intensity derived from their neighbors (employing eight-neighbor connectivity). Following the preprocessing, a 2D continuous Gabor wavelet transform was applied to detect the directional features of the image, given their predominant association with blood vessels. Strictly speaking, we computed the strongest pixel responses for different orientations, ranging from 0 to 170° in increments of 10°. This orientation sweeping was conducted for a fixed scale value of 6, which provided us with the finest vessel details. Then, a denoised image of the vessel network was reconstructed by selecting the maximum pixel intensities from all conceivable orientations (Fig. 2B). To further enhance the contrast of the vessels, we employed the Frangi filter to highlight elongated structures using the local neighborhood information derived from the eigenvalues of the Hessian matrix. Finally, the vessel centerlines were obtained by reducing their thickness into one-pixel-wide curves using a skeletonization function (Fig. 2C).

Simulation of eye model with integrated retinal vessels

The segmented vessels were integrated into the FE model of the eye to investigate their stress and strain responses. Since the vascular network is asymmetric, we utilized the three-dimensional version of the previous axisymmetric model to incorporate them (Fig. 1A). Identical material properties, loadings, and constraints were applied for this full representation of the orbit.

Component	Constitutive model	Material constants	References
Bony orbit	Linear elastic	$E = 5.37$ GPa,$\nu = 0.19$	Zhang, 2001[11]
Choroid	Neo-hookean hyperelastic	$c_{10} = 0.1$ MPa	Lam, 2023[6]
Ciliary body		$c_{10} = 1.83$ MPa	Lam, 2023[6]
Cornea		$c_{10} = 0.03967$ MPa	Zhai, 2023[12]
Lamina cribrosa		$c_{10} = 0.0233$ MPa	Edwards, 2001[13]
Lens		$c_{10} = 1.14667$ MPa	Lam, 2023[6]
Optic nerve		$c_{10} = 8.76$ kPa	Voorhees, 2020[14]
Retina		$c_{10} = 2.5$ kPa	Franze, 2011[15]
Dura mater	Yeoh's hyperelastic	$c_{10} = 0.1707$ MPa $c_{20} = 4.2109$ MPa $c_{30} = -4.9742$ MPa	Wang, 2016[7]
Sclera		$c_{10} = 0.91$ MPa $c_{20} = 19.023$ MPa $c_{30} = -64.725$ MPa	Colmenarez, 2023[16]
Orbital adipose	Neo-hookean hyperelastic, and viscoelastic	$c_{10} = 0.145055$ kPa, Prony series coefficients in the Sup. Material	Chen, 2011;[17] Schoemaker, 2006[18]

Table 1. Summary of material properties for the ocular tissues. E and ν represent the Young's modulus and Poisson's ratio, respectively. The material constants c_{ij} for $i, j = 1,2,\ldots,N$ defines the strain energy density for the hyperelastic tissues.

Parameters	Mean	Standard deviation	References
IOP (mmHg)	15.1	2.7	Wang, 2018[19]
ICP (mmHg)	11	3	Czosnyka, 2004[20]
ECP (mmHg)	140	25	Rempen, 1991[21]
Contraction time (s)	60	17	Gülümser, 2022[22]

Table 2. Means and standard deviations for the LSH from normal distributions.

To implement the vessels, we first scaled the centerline coordinates extracted from the fundus to the diameter of the retina. Then, the coordinates were manually connected by splines to the endpoints of each respective vessel. Once the centerlines were properly parametrized by a continuous curve, we perpendicularly projected them into the retina, ensuring that the vessels surrounding the optic disk, the part of the retina that connects with the optic nerve, were correctly aligned with the optic nerve. The described operations were carried out in ANSYS SpaceClaim and then exported to ABAQUS for meshing and subsequent simulation.

The vessels were modeled as one-dimensional beam elements through the Euler–Bernoulli formulations, minimizing computational burden while still retaining the capability to determine the tractional forces acting on the vessels. A transversely constant tubular profile with an external diameter of 67.5 μm and a thickness of 6.75 μm was chosen to compute the moment of inertia, required for the stress calculation. To confine the vessel's motion to the retina, we used an embedded element technique such that the translational degrees of freedom of the vessels relied solely on geometric changes of the surrounding retinal elements, while the rotational degrees of freedom remained unconstrained (ABAQUS Analysis User's Manuel). Figure 1B illustrates the arrangement of the embedded vessels within the retina model.

A worst-case NVD scenario was simulated by selecting the maximum IOP, ICP and ECP obtained from the parametric study, i.e., results when using input values of 26 mmHg for IOP, 18 mmHg for ICP, and 200 mmHg for ECP. The FE problem was solved using a static scheme to further reduce the computation time. Outcome measures were strain in the retina and optic nerve and stress in the retinal vasculature.

Results

The quantitative results of the parametric study that informed subsequent experiments are summarized in Fig. 3. Increases in both IOP and ICP shared a near 1:1 linear relationship with ECP ($m = 0.98$ and $R^2 = 0.92$ for IOP; $m = 0.96$ and $R^2 = 0.91$ for ICP). Morphological observations during the FEA simulations remained consistent regardless of exact quantitative values. On a macroscopic level, the model demonstrated that the majority of pressure applied to ocular structures originated anteriorly from direct exposure to the birth canal. Although circumferential ECP applied to the skull raised ICP, the rigid bony orbit limited the amount of pressure experienced by the contents of the orbit. In contrast, ECP could be applied to the anterior orbit and eye unimpeded. As a result, the eye was pushed posteriorly into the orbit, with the optic nerve and orbital fat providing modest resistance.

Although the optic nerve and orbital fat behind to the eye compressed and gave way as the eye was forced posteriorly, their different biomechanical properties resulted in the eye deforming nonuniformly as it was compressed. Much of the ocular tissue experienced compressive force as pressure from the birth canal's compression of the head was transferred to orbital contents. However, the dura mater, the outmost layer of optic nerve, is

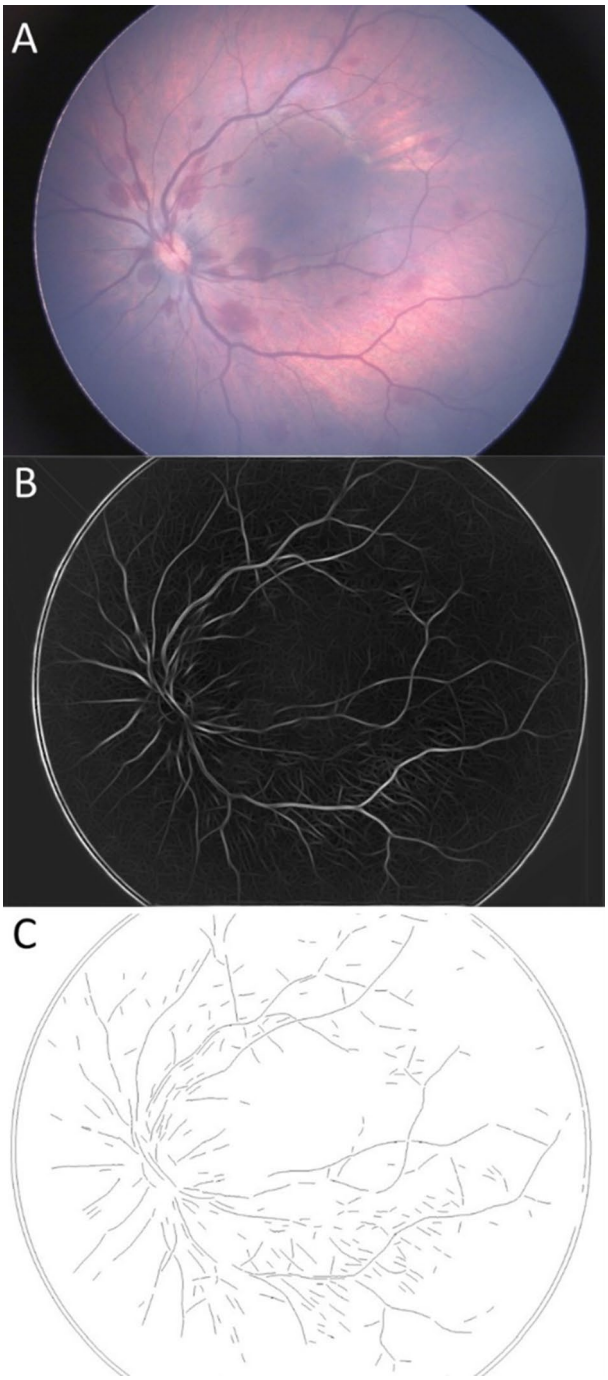

Fig. 2. Progression of image segmentation (extraction) of retinal vessels from a fundus (retinal) image exhibiting retinal hemorrhage following NVD. (**A**) Original fundus photo. (**B**) Increasing vessel contrast and performing wavelet transform segmentation. (**C**) Reduction of segmented vessels into lines for import into simulation software.

among the stiffest structures within the orbit and therefore exerted localized constraint of the eye's posterior displacement while the surrounding orbital fat permitted greater displacement (Fig. 4A). This difference in displacement resulted in tension being applied to the ocular tissue surrounding the insertion point of the optic nerve to the eye, including the peripapillary retina. These tissues experienced a strain of as great as 0.025, representing being stretched 2.5% of their original resting state (Fig. 4B). Heterogenous deformation of the eye also resulted in corresponding stresses in the retinal vasculature (Fig. 5). In the peripheral (far from the center) retina, vessel walls were exposed to compressive stress of up to 3.2 kPa. In contrast, vasculature near the optic disk experienced tensile stress of up to 2.3 kPa due to the stretching of peripapillary tissues.

The optic nerve was subjected to competing forces throughout fetal head compression. Increased ICP exerted a mean external pressure of 0.020 MPa on the optic nerve via the communicating optic nerve sheath.

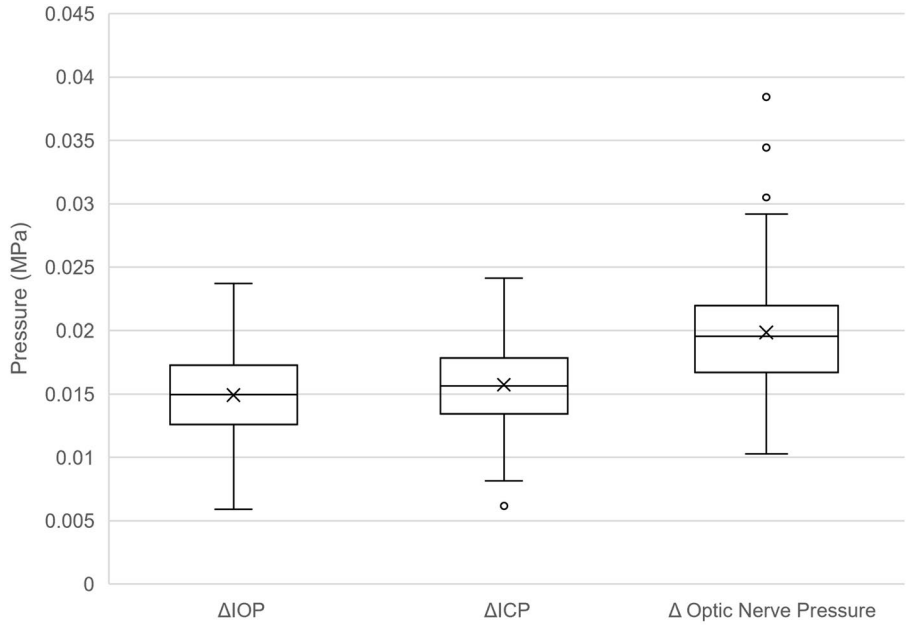

Fig. 3. Box and whisker plot demonstrating the range and distribution of changes in IOP, ICP, and optic nerve pressure observed during the parametric study of NVD.

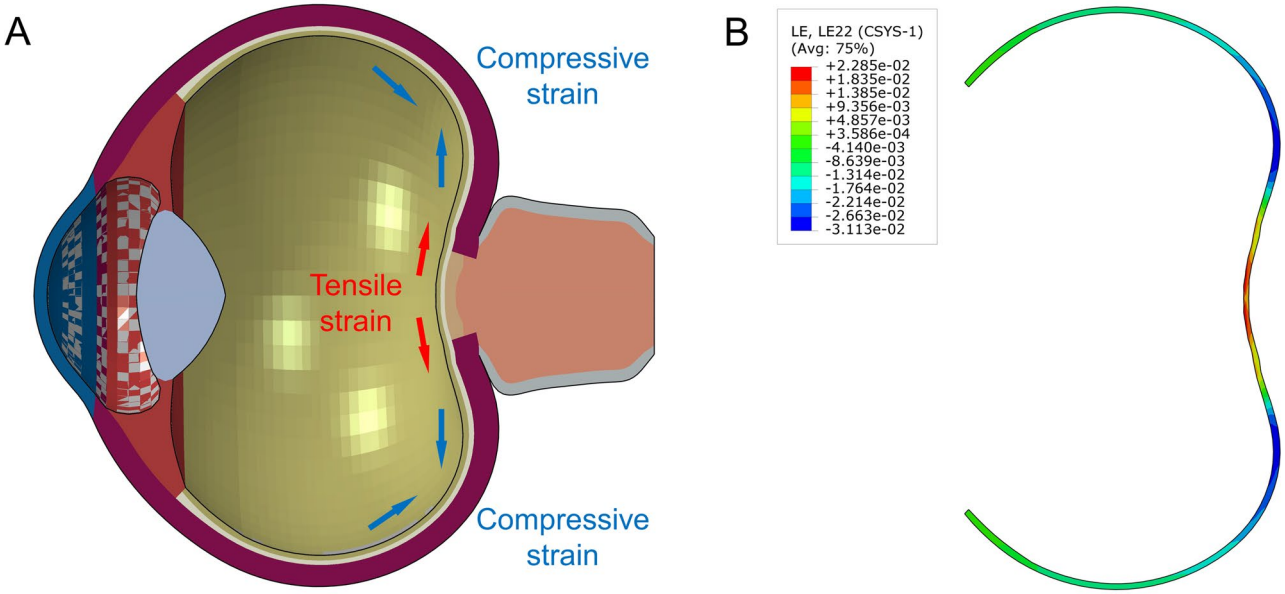

Fig. 4. Retina deformation under ECP compression of the eye. (**A**) Sagittal (side view) cross section of the eye model experiencing force during maternal contraction. Posterior tissues including the retina experience compressive or tensile strain depending on proximity to the optic nerve as labeled. Deformation of the eye is exaggerated by a scale factor of 6 for illustrative purposes. (**B**) Heatmap of strain distribution of the retina in the corresponding sagittal cross section, measured as a unitless ratio of tissue length after and before insult. "LE22" represents strain along the circumferential direction. Warmer colors (positive values) indicate tensile strain, whereas cooler colors (negative values) indicate compressive strain.

Simultaneously, posterior displacement of the eye compressed the optic nerve longitudinally, causing it to bulge transversally and experience outward tensile strain (Fig. 6). The net effect of these radially opposed forces was a mean increase in optic nerve diameter of 2.0%, though local expansion varied and reached as high as 6.1% at the intracanalicular region, where the nerve passes through the bony orbit along its path to the brain.

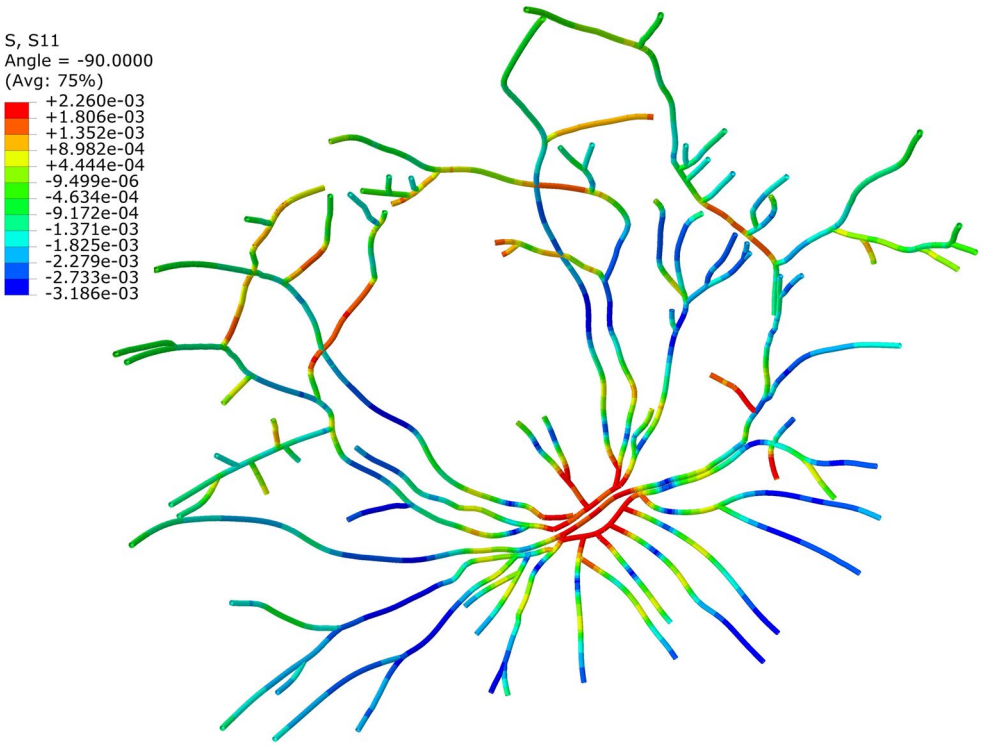

Fig. 5. Heatmap of distribution of stress in retinal veins during maternal contraction, measured in MPa. "S11" represents axial stress along the direction of the vessel. Warmer colors (positive values) indicate tensile stress, whereas cooler colors (negative values) indicate compressive stress.

Fig. 6. Heatmap of strain distribution in the optic nerve (sagittal cross section; distal (closer to the eye) end to the left of the image, proximal (closer to the brain) end to the right), measured as a unitless ratio of tissue length after and before insult. "LE11" represents strain along the radial, i.e., transversal, direction. Warmer colors (positive values) indicate tensile strain, whereas cooler colors (negative values) indicate compressive strain.

Discussion

The FEA simulation revealed that during fetal head compression associated with NVD, the retina experiences a variety of forces that stresses the vasculature simultaneously. One type of force, mechanical deformation of the eye, results in compression in the peripheral retina and traction in the peripapillary retina. This may account for the tendency of neonatal retinal hemorrhage to occur centrally, in the back of the eye, as compression of blood vessels is not usually associated with rupture and is classically associated with stopping hemorrhage[24]. In comparison, traction on vessel walls is more likely to rupture them similar to vitreous hemorrhage caused by posterior vitreous detachment, where the retina detaches from the gel-like vitreous humor that fills the back of the eye. The 2.3 kPa observed in this simulation falls within the range of 1–5 kPa necessary to induce separation of the retina from the vitreous in sheep, suggesting ample force to tear the retinal vessels[25]. Elevated blood pressure, which was not modeled due to simulation constraints in the embedded elements, can also induce internal tensile stress within the retinal vessels, contributing to the total strain on the most affected vessel walls, and the formation of a tear.

Smaller vessels such as venules and capillaries, which are not directly visualized in this simulation due to their exponential complexity and thus computational burden compared to larger vessels, likely account for much of the observed hemorrhage due to the proportionally greater impact of the forces. The thinner walls of the smaller vessels render them more vulnerable to the mechanical deformation of the retina and thus more likely to rupture

compared to larger veins and their thicker, muscle-lined arterial counterparts. The majority of neonatal retinal hemorrhages localizing to the intraretinal layer may suggest disruption of the deep capillary plexus, a high-density network of capillaries which resides between the inner nuclear and outer plexiform layers of the retina[26].

The blood vessels within the retina arise from the central retinal artery and veins, which course through the optic nerve. In this simulation, the optic nerve experienced a net expansion in diameter due to axial compression and consequent bulging. The transverse expansion is greatest in the proximal nerve at the intracanalicular region due to displacement being constrained, which mimics the tethering of the optic nerve sheath to the periosteum lining of the surrounding bone that forms the canal[27]. This result subverted expectations of a reduction in diameter resulting from external compression associated with increasing ICP. Previously suggested mechanisms of retinal hemorrhage during NVD proposed obstruction of venous blood drainage at the central retinal vein or further proximal during head compression, resulting in buildup of pressure in distal retinal veins and capillaries[1,4,5]. That the diameter of the optic nerve not only fails to decrease appreciably, but rather increases, suggests that any compression of the central retinal vein is unlikely, let alone sufficient enough to result in venous congestion. This aligns with concurrent retinal venous abnormalities associated with outflow blockage such as engorgement or tortuosity being considered atypical in literature pertaining to neonatal retinal hemorrhage[28]. Therefore, the mechanism of retinal hemorrhage in this setting is more likely due to mechanical deformation applying stress to vessel walls as opposed to venous occlusion.

Although neonatal retinal hemorrhage is exceedingly common, especially in instrument-assisted deliveries, investigations into the pathophysiology are scarce given the invasive nature of monitoring childbirth. The present analysis aimed to examine this elusive topic but also serve as a proof-of-concept for the efficient simulation of blood vessels to study disease of potentially vascular etiology. These advances were enabled by methodological modifications made to maximize efficiency of high-resolution computer simulations such as use of an axisymmetric model, performing the parametric study with the LHS scheme, and modeling of vessels through Euler–Bernoulli formulations. Such continuous refinement of protocols in combination with more powerful graphics processing units becoming commercially available will allow for future experiments involving the anatomically complex eye to be conducted in even greater detail.

Limitations of this study include the challenge of emulating in vivo conditions as closely as possible within the confines of a computer simulation. While the model presented was constructed using the most precise biomechanical property data available in the literature, normal vaginal delivery is a process with wide variance; factors such as strength of contractions, systemic considerations like the impact of neonatal sympathetic nervous system activation on blood pressure, and the morphology of both the birth canal and neonate are unique to every delivery. Furthermore, only major vessels were visualized due to aforementioned computational restraints; additional efficiency gains and acquisition of cutting-edge hardware will be necessary investments to simulate models at the capillary level. However, while refining these parameters would most likely serve to improve quantitative accuracy, the macroscopic trends that this study sought to uncover are unlikely to change. As such, FEA simulations continue to offer a noninvasive medium to investigate difficult-to-study phenomena such as neonatal retinal hemorrhage.

Despite limitations inherent to computer simulations, the present model builds upon previous work and represents our most detailed and accurate model to date. Organically deriving ICP from the skull's reaction to ECP allowed for more accurate differentials in local pressure within the eye and orbit, in turn revealing the nature of the backward displacement and deformation of the eye. Furthermore, improvements to simulation methodology enabled the addition of retinal vasculature, previously too detailed to study efficiently. This direct visualization of mechanical forces on the retinal vasculature is, to the best of the authors' knowledge, the first investigation of vessel biomechanics in the context of neonatal retinal hemorrhage reported in the literature and may serve as a foundation for future research into retinal pathophysiology.

Data availability

The datasets generated during and/or analyzed during the current study are available from the corresponding author on reasonable request.

Received: 11 June 2024; Accepted: 28 August 2024
Published online: 26 November 2024

References

1. Callaway, N. F. *et al.* Retinal and optic nerve hemorrhages in the newborn infant. *Ophthalmology* **123**, 1043–1052 (2016).
2. Kim, S. Y. & Suh, D. W. Comparison of the characteristics of retinal hemorrhages in abusive head trauma versus normal vaginal delivery. *J. Am. Assoc. Pediatr. Ophthalmol. Strabismus* **21**, e24 (2017).
3. Emerson, M. V., Pieramici, D. J., Stoessel, K. M., Berreen, J. P. & Gariano, R. F. *Incidence and Rate of Disappearance of Retinal Hemorrhage in Newborns*.
4. Watts, P. *et al.* Newborn retinal hemorrhages: A systematic review. *J. Am. Assoc. Pediatr. Ophthalmol. Strabismus* **17**, 70–78 (2013).
5. Zhao, Q. *et al.* Birth-related retinal hemorrhages in healthy full-term newborns and their relationship to maternal, obstetric, and neonatal risk factors. *Graefes Arch. Clin. Exp. Ophthalmol.* **253**, 1021–1025 (2015).
6. Lam, M. R. *et al.* The role of intrapartum fetal head compression in neonatal retinal hemorrhage. *J. Am. Assoc. Pediatr. Ophthalmol. Strabismus* https://doi.org/10.1016/j.jaapos.2023.07.013 (2023).
7. Wang, X. *et al.* Finite element analysis predicts large optic nerve head strains during horizontal eye movements. *Investig. Ophthalmol. Vis. Sci.* **57**, 2452 (2016).
8. Feola, A. J. *et al.* Finite element modeling of factors influencing optic nerve head deformation due to intracranial pressure. *Investig. Ophthalmol. Vis. Sci.* **57**, 1901 (2016).
9. Rossi, T. *et al.* The pathogenesis of retinal damage in blunt eye trauma: finite element modeling. *Investig. Ophthalmol. Vis. Sci.* **52**, 3994–4002 (2011).
10. Myron Yanoff, J. W. S. *Ocular Pathology* (Elsevier, 2015). https://doi.org/10.1016/C2010-0-68524-5.

11. Zhang, L., Yang, K. H. & King, A. I. Comparison of brain responses between frontal and lateral impacts by finite element modeling. *J. Neurotrauma* **18**, 21–30 (2001).
12. Zhai, Y. *et al.* Multiscale Mechanical Characterization of Cornea With AFM, SEM, and Uniaxial Tensile Test. In *Volume 5: Biomedical and Biotechnology* V005T06A010 (American Society of Mechanical Engineers, 2023). https://doi.org/10.1115/IMECE2023-113394.
13. Edwards, M. E. & Good, T. A. Use of a mathematical model to estimate stress and strain during elevated pressure induced lamina cribrosa deformation. *Curr. Eye Res.* **23**, 215–225 (2001).
14. Voorhees, A. P. *et al.* So-called lamina cribrosa defects may mitigate IOP-induced neural tissue insult. *Investig. Ophthalmol. Vis. Sci.* **61**, 15 (2020).
15. Franze, K. *et al.* Spatial mapping of the mechanical properties of the living retina using scanning force microscopy. *Soft Matter* **7**, 3147 (2011).
16. Colmenarez, J. *et al.* Damage-induced softening of the sclera: A pseudo-elastic modeling approach. *J. Eng. Sci. Med. Diagn. Ther.* https://doi.org/10.1115/1.4063467 (2023).
17. Chen, K. & Weiland, J. D. Mechanical properties of orbital fat and its encapsulating connective tissue. *J. Biomech. Eng.* **133**, 064505 (2011).
18. Schoemaker, I. *et al.* Elasticity, viscosity, and deformation of orbital fat. *Investig. Ophthalmol. Vis. Sci.* **47**, 4819 (2006).
19. Wang, Y. X., Xu, L., Wei, W. B. & Jonas, J. B. Intraocular pressure and its normal range adjusted for ocular and systemic parameters. The Beijing Eye Study 2011. *PLoS One* **13**, e0196926 (2018).
20. Czosnyka, M. Monitoring and interpretation of intracranial pressure. *J. Neurol. Neurosurg. Psychiatry* **75**, 813–821 (2004).
21. Rempen, A. & Kraus, M. Measurement of head compression during labor: Preliminary results. *JPME* **19**, 115–120 (1991).
22. Gülümser, C., Yassa, M., WHO Intrapartum Care Algorithms Working Group. Clinical management of uterine contraction abnormalities; An evidence-based intrapartum care algorithm. *BJOG* https://doi.org/10.1111/1471-0528.16727 (2022).
23. Soares, J. V. B., Leandro, J. J. G., Cesar, R. M., Jelinek, H. F. & Cree, M. J. Retinal vessel segmentation using the 2-D Gabor wavelet and supervised classification. *IEEE Trans. Med. Imaging* **25**, 1214–1222 (2006).
24. Lakstein, D. *et al.* Tourniquets for Hemorrhage control on the battlefield: A 4-year accumulated experience. *J. Trauma Inj. Infect. Crit. Care* **54**, S221–S225 (2003).
25. Song, H. H. *et al.* Exploring the vitreoretinal interface: A key instigator of unique retinal hemorrhage patterns in pediatric head trauma. *Korean J. Ophthalmol.* **36**, 253–263 (2022).
26. Campbell, J. P. *et al.* Detailed vascular anatomy of the human retina by projection-resolved optical coherence tomography angiography. *Sci. Rep.* **7**, 42201 (2017).
27. Yu-Wai-Man, P. Traumatic optic neuropathy—Clinical features and management issues. *Taiwan J. Ophthalmol.* **5**, 3–8 (2015).
28. Cho, I. H., Kim, M. S., Heo, N. H. & Kim, S. Y. Birth-related retinal hemorrhages: The Soonchunhyang University Cheonan Hospital universal newborn eye screening (SUCH-NES) study. *PLoS One* **16**, e0259378 (2021).

Author contributions

Conceptualization: M.R.L., J.A.C, D.W.S.; data curation: J.A.C., M.R.L.; formal analysis: J.A.C., M.R.L., D.W.S.; investigation: M.R.L., J.A.C.; methodology: J.A.C., M.R.L., L.G.; project administration: M.R.L., J.A.C.; resources: J.A.C., P.D., L.G.; software: J.A.C., P.D., L.G.; supervision: P.D., L.G., D.W.S.; validation: P.D., L.G., D.W.S.; visualization: J.A.C., M.R.L.; writing—original draft: M.R.L., J.A.C.; writing—review and editing: M.R.L., J.A.C., P.D., L.G., D.W.S.

Competing interests

The authors declare no competing interests.

Additional information

Supplementary Information The online version contains supplementary material available at https://doi.org/10.1038/s41598-024-71509-w.

Correspondence and requests for materials should be addressed to L.G. or D.W.S.